



# Room-temperature ferromagnetism in $C^+$ -implanted AlN films

Cite as: Appl. Phys. Lett. **115**, 262401 (2019); <https://doi.org/10.1063/1.5131036>

Submitted: 08 October 2019 . Accepted: 09 December 2019 . Published Online: 23 December 2019

R. Ye , J. D. Liu, H. J. Zhang , and B. J. Ye



View Online



Export Citation



CrossMark

## ARTICLES YOU MAY BE INTERESTED IN

[Fine structure of another blue luminescence band in undoped GaN](#)

Applied Physics Letters **115**, 262102 (2019); <https://doi.org/10.1063/1.5126803>

[Physical mechanism on the suppression of dynamic resistance degradation by multi-mesa-channel in AlGaIn/GaN high electron mobility transistors](#)

Applied Physics Letters **115**, 262101 (2019); <https://doi.org/10.1063/1.5132991>

[Terahertz intersubband absorption of GaN/AlGaIn step quantum wells grown by MOVPE on Si\(111\) and Si\(110\) substrates](#)

Applied Physics Letters **115**, 261103 (2019); <https://doi.org/10.1063/1.5129362>

Lock-in Amplifiers  
Find out more today



Zurich  
Instruments

# Room-temperature ferromagnetism in C<sup>+</sup>-implanted AlN films

Cite as: Appl. Phys. Lett. **115**, 262401 (2019); doi: [10.1063/1.5131036](https://doi.org/10.1063/1.5131036)

Submitted: 8 October 2019 · Accepted: 9 December 2019 ·

Published Online: 23 December 2019




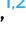

View Online



Export Citation



CrossMark

R. Ye,<sup>1,2</sup>  J. D. Liu,<sup>1,2,a)</sup>  H. J. Zhang,<sup>1,2</sup>  and B. J. Ye<sup>1,2,b)</sup>

## AFFILIATIONS

<sup>1</sup>Hefei National Laboratory for Physical Sciences at the Microscale, University of Science and Technology of China, Hefei 230026, China

<sup>2</sup>State Key Laboratory of Particle Detection and Electronics, University of Science and Technology of China, Hefei 230026, China

<sup>a)</sup>Electronic mail: [liujd@ustc.edu.cn](mailto:liujd@ustc.edu.cn)

<sup>b)</sup>Electronic mail: [bjye@ustc.edu.cn](mailto:bjye@ustc.edu.cn)

## ABSTRACT

Diluted magnetic semiconductors (DMSs) have numerous potential applications, particularly in spintronics. Therefore, the search for advanced DMSs has been a critical task for a long time. In this work, room-temperature ferromagnetism is observed in the C<sup>+</sup>-implanted AlN films with C<sup>+</sup> doses of  $5 \times 10^{16}$  (AlN:C<sub>5×10<sup>16</sup></sub>) and  $2 \times 10^{17}$  cm<sup>-2</sup> (AlN:C<sub>2×10<sup>17</sup></sub>). AlN:C<sub>2×10<sup>17</sup></sub> exhibits a saturation magnetization of ~0.104 emu/g, nearly 1.5 times that of AlN:C<sub>5×10<sup>16</sup></sub>. X-ray diffraction and X-ray photoelectron spectroscopy (XPS) measurements reveal that the implanted C<sup>+</sup> ions occupy the interstitial lattice sites and substitute at the sites of Al atoms. XPS and Doppler broadening of positron annihilation radiation measurements demonstrate the existence of the Al-vacancy related defects in the C<sup>+</sup>-implanted AlN films. First-principles calculations indicate that the ferromagnetism in AlN:C<sub>5×10<sup>16</sup></sub> and AlN:C<sub>2×10<sup>17</sup></sub> is mainly originated from defect complexes involving interstitial C atoms and Al vacancies, which have the lowest formation energy among AlN:C defects containing C atoms and Al vacancies. This work provides a feasible route to develop advanced DMSs.

Published under license by AIP Publishing. <https://doi.org/10.1063/1.5131036>

Diluted magnetic semiconductors (DMSs) have attracted considerable attention due to their potential applications in spintronics.<sup>1</sup> In the past several, room-temperature ferromagnetism has been investigated in several types of semiconducting oxides and nitrides, such as ZnO,<sup>2</sup> TiO<sub>2</sub>,<sup>3</sup> SnO<sub>2</sub>,<sup>4</sup> GaN,<sup>5,6</sup> and AlN.<sup>7</sup>

AlN, a wide-bandgap III–IV semiconductor, is one of the most promising spintronic materials because of its high thermal conductivity, high electron mobility, and good chemical stability. Recently, many groups have reported the observation of room-temperature ferromagnetism in AlN DMSs doped with magnetic transition metals such as Mn, Fe, Cr, and Ni.<sup>8–11</sup> However, the origin of the ferromagnetism in the magnetic transition metal-doped AlN DMSs remains controversial; it is unclear whether the ferromagnetism is attributed to the intrinsic properties of the DMSs or extrinsic impurities (magnetic clusters or secondary phases).<sup>12</sup> Gao *et al.* revealed that the ferromagnetism in the Fe-doped AlN films arises from the AlFeN ternary alloy.<sup>9</sup> In contrast, Zhang *et al.* suggested that defects such as nitrogen vacancies and their associated bound magnetic polarons may play a critical role in the ferromagnetic properties of the Cr-doped AlN films.<sup>13</sup> These discrepancies have led to searches for AlN DMSs based on nonmagnetic elements. A promising strategy to identify the origin of

ferromagnetism is to introduce ferromagnetic properties in AlN DMSs via nonmagnetic dopants since the precipitation of nonmagnetic dopants does not contribute to ferromagnetism. In this case, the ferromagnetic property could be identified as intrinsic. The magnetic properties of the C-doped AlN have been investigated by theoretical calculations,<sup>14</sup> and the results suggest the possibility of ferromagnetism in the C-doped AlN. However, ferromagnetism has not been experimentally observed in the C-doped AlN so far.

In this study, we prepared the C-doped AlN DMS films via C<sup>+</sup> ion implantation. The structural and magnetic properties of the C<sup>+</sup>-implanted AlN films were investigated through various experiments. First-principles calculations based on density functional theory (DFT) revealed that the ferromagnetism most likely arises from defect complexes involving interstitial C atoms and Al vacancies.

AlN films with thicknesses of 1 μm (marked as as-grown AlN) prepared on *c*-plane (0001) sapphire substrates (~500 μm thick) using hydride vapor phase epitaxy were purchased from Hefei Kejing Materials Technology Co., Ltd. AlN:C<sub>5×10<sup>16</sup></sub> and AlN:C<sub>2×10<sup>17</sup></sub> (the subscript denotes the dose of the implanted C<sup>+</sup> ions in cm<sup>-2</sup>) were obtained by implanting C<sup>+</sup> ions with an energy of 80 keV into two as-grown AlN films with dimensions of 6 × 8 mm<sup>2</sup>. Ion implantation

was performed using an ion implanter at room temperature. The base pressure of the implantation chamber was approximately  $2 \times 10^{-4}$  Pa.

X-ray diffraction (XRD) measurements of the AlN films were conducted using an X-ray diffractometer (PANalytical X'Pert PRO MPD) with Cu-K $\alpha$  radiation ( $\lambda = 1.5406$  Å). X-ray photoelectron spectroscopy (XPS) experiments were carried out using a Thermo-Science ESCALAB 250Xi spectrometer. Before recording the XPS data, the AlN films were sputtered with an Ar<sup>+</sup> ion source operated at 3 kV for 90 s. The Doppler broadening of annihilation radiation (DBAR) measurements was performed using a slow positron beam with a variable energy from 0.25 to 20 keV at the University of Science and Technology of China. The magnetic properties of the AlN films were investigated using a Superconducting Quantum Interference Device (MPMS3, Quantum Design). The magnetic hysteresis loops were measured at room temperature with the magnetic field parallel to the plane of the samples. Field-cooled (FC) and zero-field-cooled (ZFC) measurements were conducted at an applied magnetic field intensity of 1000 Oe in the temperature range of 4–300 K.

The crystal structures of the AlN samples were evaluated by XRD. The XRD spectra were normalized with respect to the intensity of the (0006) peak of the sapphire substrate for the as-grown AlN sample. As shown in Fig. 1, the typical (002) and (004) peaks of AlN are observed, which can be indexed to the hexagonal wurtzite structure of AlN (JCPDS 65-0832). No peaks related to Al<sub>3</sub>C<sub>4</sub> or metallic Al are found in the XRD spectra. As shown in the inset of Fig. 1, the intensity of the AlN (002) peak decreased after ion implantation, indicating that implantation introduced numerous lattice defects in AlN:C<sub>5</sub>×10<sup>16</sup> and AlN:C<sub>2</sub>×10<sup>17</sup>. Shifts in the AlN (002) peaks were observed in the spectra of AlN:C<sub>5</sub>×10<sup>16</sup> and AlN:C<sub>2</sub>×10<sup>17</sup>, indicating a variation in the lattice parameter *c*. In general, a lattice contraction would be expected when the Al<sup>3+</sup> sites are substituted by the C<sup>+</sup> ions due to the smaller covalent radius of C; in contrast, the lattice expansion is expected to occur when the C<sup>+</sup> ions occupy interstitial lattice sites.<sup>15</sup> As shown in Table I, the *c* parameter indicates a lattice contraction in AlN:C<sub>5</sub>×10<sup>16</sup>, suggesting that most C<sup>+</sup> ions occupy the substitutional sites of Al<sup>3+</sup>, while a few incorporate at the interstitial sites. As the dose of implanted C<sup>+</sup> ions increases threefold, the lattice parameter increases

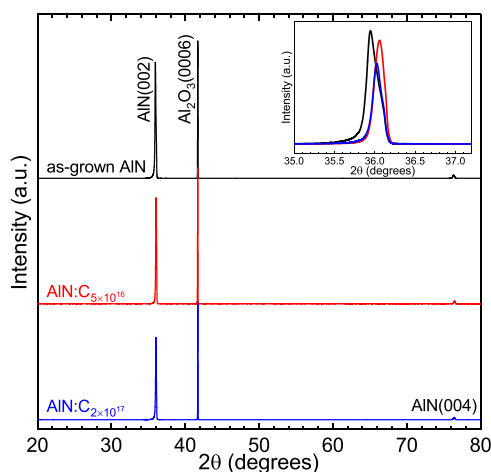


FIG. 1. XRD patterns of the as-grown AlN, AlN:C<sub>5</sub>×10<sup>16</sup>, and AlN:C<sub>2</sub>×10<sup>17</sup>. The inset shows the magnification of AlN (002) peaks.

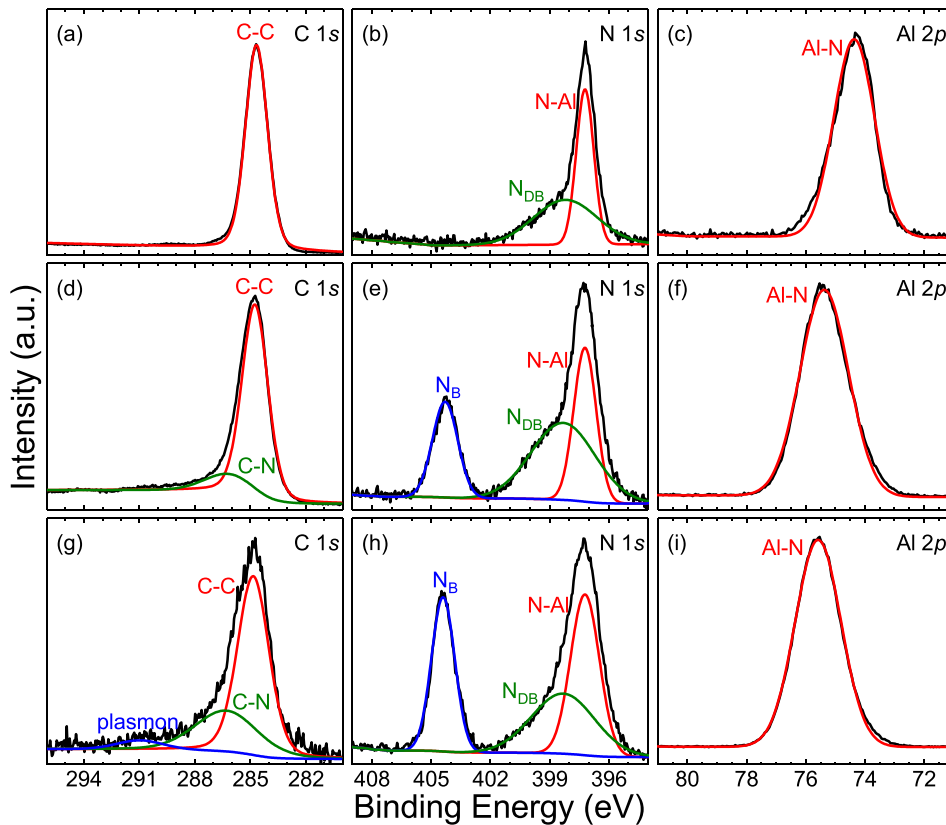
TABLE I. XRD results of the AlN samples.

Sample	Peak position (°)		<i>c</i> Parameter (Å)
	(002)	(004)	
As-grown AlN	35.95	76.34	4.992
AlN:C <sub>5</sub> ×10 <sup>16</sup>	36.06	76.47	4.977
AlN:C <sub>2</sub> ×10 <sup>17</sup>	36.04	76.43	4.981

slightly for AlN:C<sub>2</sub>×10<sup>17</sup>, which is likely attributed to the generation of more interstitial C atoms along with the limited substitution of Al<sup>3+</sup> by the C<sup>+</sup> ions.

To analyze the chemical structures of the AlN samples, XPS measurements were performed. The XPS C 1s, N 1s, and Al 2*p* core-level spectra of the AlN films are shown in Fig. 2. The core-level spectra were deconvoluted using XPSPEAK 4.1 software<sup>16</sup> to determine the bonding states. In Fig. 2(a), only a single peak is observed at around 284.8 eV. This peak (corresponding to the C–C bonding states) was used as a standard to calibrate the peaks in other spectra. In Figs. 2(d) and 2(g), the chemical states at the binding energy of approximately 286.2 eV are associated with the C–N bonds, which reveals that the C<sup>+</sup> ions occupy the Al<sup>3+</sup> substitutional sites and the interstitial lattice sites in AlN:C<sub>5</sub>×10<sup>16</sup> and AlN:C<sub>2</sub>×10<sup>17</sup>. In the N 1s core-level spectra [Figs. 2(b), 2(e), and 2(h)], the fitted peaks located at binding energies of 397.2, 398.2, and 404.3 eV are attributed to N–Al, N dangling bonds (N<sub>DB</sub>),<sup>17–19</sup> and nitrogen bubbles (N<sub>D</sub>),<sup>18–20</sup> respectively. The intensity of the N<sub>DB</sub> peak increases after implantation with the breaking of N–Al bonds, suggesting that the C<sup>+</sup> implantation may induce more Al-related vacancies in AlN:C<sub>5</sub>×10<sup>16</sup> and AlN:C<sub>2</sub>×10<sup>17</sup>. As shown in Figs. 2(c), 2(f), and 2(i), the binding energies of the Al 2*p* states for the as-grown AlN, AlN:C<sub>5</sub>×10<sup>16</sup>, and AlN:C<sub>2</sub>×10<sup>17</sup> are 74.4, 75.4, and 75.6 eV, respectively, which all correspond to the Al–N bonds. The Al 2*p* peaks of AlN:C<sub>5</sub>×10<sup>16</sup> and AlN:C<sub>2</sub>×10<sup>17</sup> shift ~1 eV toward a higher binding energy, indicating the presence of the interstitial C atoms around the Al atoms in the Al–N bonds.<sup>21</sup> This finding is consistent with the XRD results.

To investigate the microstructural defects in the AlN samples, the DBAR spectra were measured and characterized by the *S* and *W* parameters. The *S* and *W* parameters are defined as the ratio of annihilation events in the central region (510.19–511.81 keV) and the wing regions (505.92–509.16 keV and 512.84–516.08 keV) of the annihilation peak to the total counts, respectively. Plots of the *S* parameter vs positron energy *E* for the samples are shown in Fig. 3(a). For the as-grown AlN, positron energies in the range of 0–2.5 keV correspond to the surface layer.<sup>22</sup> In the surface layer, the *S* parameter decreases with an increasing positron energy. The value of the *S* parameter is saturated in the positron energy range of 2.5–9.0 keV, indicating that all positrons are annihilated in the AlN layer. The obtained bulk *S* parameter (*S*<sub>b</sub>) for the as-grown AlN is approximately 0.439. The *S* parameter then decreases in the high energy region *E* > 9.0 keV due to the increasing fraction of the annihilation of positrons in the sapphire substrate.<sup>23</sup> As shown by the upper horizontal axis of Fig. 3(a), the defect layers for AlN:C<sub>5</sub>×10<sup>16</sup> and AlN:C<sub>2</sub>×10<sup>17</sup> range from approximately 37 to 166 nm, corresponding to the positron energy range of 2.0–5.0 keV. The depth of the defect layer is within the reasonable range of the Stopping and Ranges of Ions in Matter (SRIM) simulation results (20–250 nm; see Fig. S1). Compared to the as-grown AlN, the C<sup>+</sup>-implanted AlN films show much higher *S* parameters in the



**FIG. 2.** XPS core-level spectra of C 1s, N 1s, and Al 2p for (a)–(c) the as-grown AlN, (d)–(f) AlN:C<sub>5</sub>×10<sup>16</sup>, and (g)–(i) AlN:C<sub>2</sub>×10<sup>17</sup>. The black solid lines represent the original XPS data. The red, green, and blue solid lines represent the fitted bonding states.

defect layers, which is attributed to the annihilation of positrons in vacancy-type defects introduced by the C<sup>+</sup> implantation. In addition, since more positrons diffuse backward to the defect layers in AlN:C<sub>5</sub>×10<sup>16</sup> and AlN:C<sub>2</sub>×10<sup>17</sup>, the *S*–*E* curves of AlN:C<sub>5</sub>×10<sup>16</sup> and AlN:C<sub>2</sub>×10<sup>17</sup> in the high energy region are not overlapped with that of the as-grown AlN. These cases are similar to those of the Mn<sup>+</sup>-implanted TiO<sub>2</sub>.<sup>24</sup> The effective positron trapping centers in AlN are the Al-related vacancies (negative charges). The defect types in AlN:C<sub>5</sub>×10<sup>16</sup> and AlN:C<sub>2</sub>×10<sup>17</sup> can be determined by the *S* parameters. The *S* parameters for the defect layers (*S*<sub>d</sub>) in AlN:C<sub>5</sub>×10<sup>16</sup> and AlN:C<sub>2</sub>×10<sup>17</sup> are 0.457 and 0.461, respectively, corresponding to the *S*<sub>d</sub>/*S*<sub>b</sub> values of approximately 1.041 and 1.050, respectively. This indicates that the implantation-induced defects in AlN:C<sub>5</sub>×10<sup>16</sup> and AlN:C<sub>2</sub>×10<sup>17</sup> are probably monovacancies (V<sub>Al</sub>) or divacancies according to the previous reports.<sup>25,26</sup>

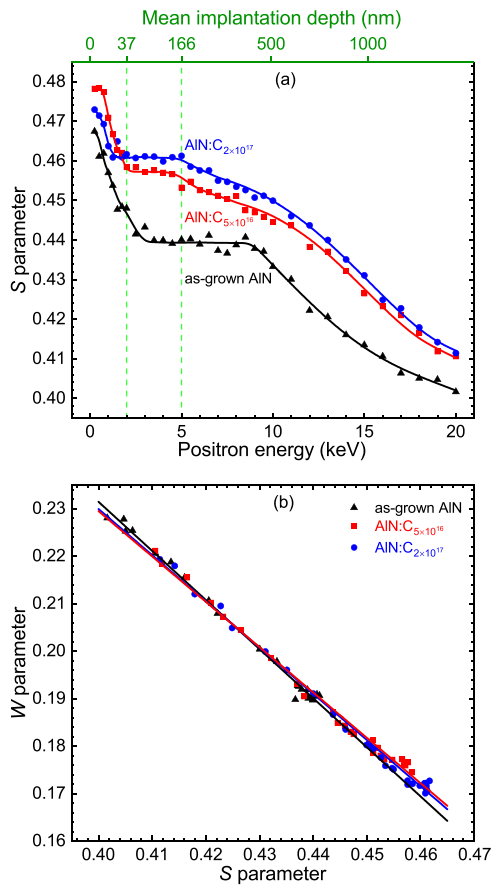
The change in the defect type can be further characterized based on the *S*–*W* curves; a change in the slope of the linear *S*–*W* relationship is closely related to the variation in the defect type.<sup>27,28</sup> The *S*–*W* curves for AlN:C<sub>5</sub>×10<sup>16</sup> and AlN:C<sub>2</sub>×10<sup>17</sup> are shown in Fig. 3(b). The *S*–*W* data for positron energies below 2.0 keV were subtracted. The fitting lines of the *S*–*W* data for the as-grown AlN, AlN:C<sub>5</sub>×10<sup>16</sup>, and AlN:C<sub>2</sub>×10<sup>17</sup> are approximately coincident, indicating that these samples contain the same types of defects. Therefore, increasing the dose of C<sup>+</sup> ions increases the density of the Al-related vacancies but does not change the defect type.

The magnetization (*M*) as a function of the applied magnetic field (*H*) is shown for the as-grown AlN, AlN:C<sub>5</sub>×10<sup>16</sup>, and AlN:

C<sub>2</sub>×10<sup>17</sup> in Fig. 4(a). The as-grown AlN exhibits an almost-zero hysteresis phenomenon, indicating the absence of magnetic impurities in the as-grown AlN. However, distinct S-shaped hysteresis loops are observed for AlN:C<sub>5</sub>×10<sup>16</sup> and AlN:C<sub>2</sub>×10<sup>17</sup>, suggesting that these samples are ferromagnetic. As shown in the inset in Fig. 4(b), the remanent magnetization of AlN:C<sub>2</sub>×10<sup>17</sup> (AlN:C<sub>5</sub>×10<sup>16</sup>) is approximately 0.0215 emu/g (0.0096 emu/g), the saturation magnetization (*M*<sub>S</sub>) is about 0.104 emu/g (0.072 emu/g), and the coercive field is about 130 Oe (108 Oe). The weak coercive fields are quite similar to those that have been reported in other DMSs.<sup>6,29</sup>

The temperature dependences of the FC and ZFC magnetizations were measured for AlN:C<sub>2</sub>×10<sup>17</sup>, as shown in Fig. 4(b). As shown in the FC/ZFC curves, the magnetization decreases slowly as the temperature increases from 5 to 300 K. Neither platforms nor transition peaks are observed in the FC/ZFC curves, indicating that AlN:C<sub>2</sub>×10<sup>17</sup> has no spin glass or superparamagnetic properties. The inset in Fig. 4(b) shows the temperature dependence of the difference in the magnetization between FC and ZFC. The difference remains above zero as the temperature increases to 300 K, indicating that the hysteretic phenomenon observed in AlN:C<sub>2</sub>×10<sup>17</sup> can be attributed to the ferromagnetism.

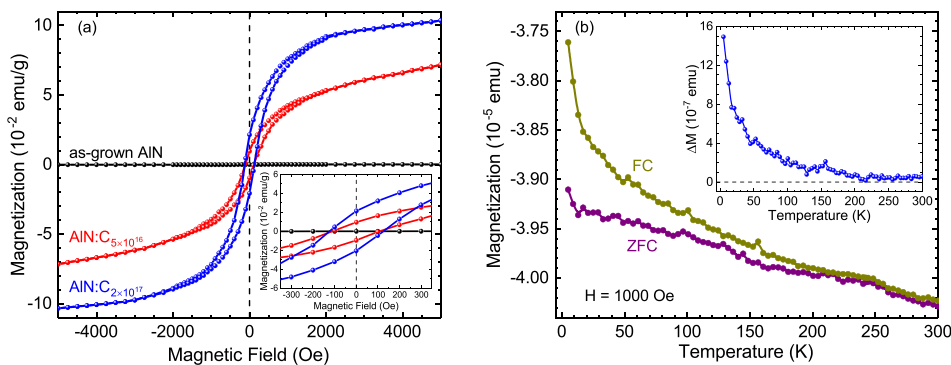
The as-grown AlN exhibits no ferromagnetic properties, while the *M*<sub>S</sub> value of AlN:C<sub>2</sub>×10<sup>17</sup> is almost 1.5 times larger than that of AlN:C<sub>5</sub>×10<sup>16</sup>, suggesting that the ferromagnetism is strongly correlated with the C<sup>+</sup> ion dose. According to the XRD and the XPS results, the possibility of secondary phases such as Al<sub>4</sub>C<sub>3</sub> can be excluded. In addition, the DBAR measurements suggest the presence of large quantities of the Al-related vacancies in AlN:C<sub>5</sub>×10<sup>16</sup> and AlN:C<sub>2</sub>×10<sup>17</sup>. Thus, we



**FIG. 3.** (a) The parameter  $S$  as a function of positron energy ( $E$ ) for the samples. The solid and the vertical dashed lines are guides for the eyes. The range of the mean implantation depth between the two vertical dashed lines corresponds approximately to the defect layers for AlN:C<sub>5</sub>×10<sup>16</sup> and AlN:C<sub>2</sub>×10<sup>17</sup>. (b) Plots of  $S$  vs  $W$  for the samples. The black, red, and blue straight lines are fits to the  $S$ - $W$  data for the as-grown AlN, AlN:C<sub>5</sub>×10<sup>16</sup>, and AlN:C<sub>2</sub>×10<sup>17</sup>, respectively.

propose that the ferromagnetism in the C<sup>+</sup>-implanted AlN films is related to the Al vacancies and the C atoms.

To obtain further insight into the ferromagnetic properties of the C<sup>+</sup>-implanted AlN films, we calculated their electronic and magnetic properties along with their formation energies using the DFT methods.



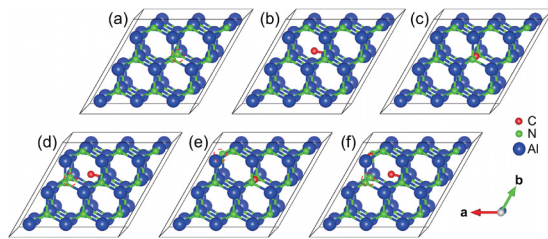
**FIG. 4.** (a) Room-temperature  $M$ - $H$  loops for the AlN samples. The inset presents the magnified  $M$ - $H$  curves in the low-field region from  $-350$  to  $350$  Oe. The diamagnetic background signals were subtracted. The magnetization values were normalized by accounting for the masses of the AlN films. (b) Temperature dependences of FC and ZFC magnetization for AlN:C<sub>2</sub>×10<sup>17</sup>. The inset shows the temperature dependence of the difference in magnetization between the FC and the ZFC curves,  $M_{FC} - M_{ZFC}$ , for AlN:C<sub>2</sub>×10<sup>17</sup>.

Our AlN samples contained various defects due to the implantation of the C<sup>+</sup> ions. In our calculations, we considered six structures with different defects that most likely exist in the AlN films: (a) an Al vacancy ( $V_{Al}$ ), (b) an interstitial C atom ( $C_i$ ), (c) a substitutional C atom at an Al site ( $C_{Al}$ ), (d) an interstitial-vacancy complex ( $C_i-V_{Al}$ ), (e) a substitutional-vacancy complex ( $C_{Al}-V_{Al}$ ), and (f) an interstitial-vacancy/substitutional complex ( $C_i-V_{Al}-C_{Al}$ ), as shown in Fig. 5. The calculated lattice parameters for the wurtzite AlN supercell are  $a = 3.111$  Å and  $c = 4.986$  Å, which are in good agreement with the experimental values.<sup>30</sup>

The total magnetic moments and the formation energies of the six AlN structures with defects (under N-rich conditions) are shown in Table II. For  $V_{Al}$ , the total magnetic moment is  $3.00 \mu_B$ , and the formation energy is  $6.902$  eV. The values are in good accordance with the results of the previous first-principles calculations by Wu *et al.*<sup>31</sup> The high formation energy would make it difficult to achieve a sufficient Al vacancy concentration at a thermal equilibrium necessary for ferromagnetism,<sup>31</sup> as in the cases of  $C_i$  and  $C_{Al}-V_{Al}$ . For  $C_{Al}$  and  $C_i-V_{Al}-C_{Al}$ , the calculated total magnetic moment is  $0 \mu_B$ , indicating that these defects do not contribute to the ferromagnetism.  $C_i-V_{Al}$ , which has a magnetic moment of  $1.00 \mu_B$ , has the lowest formation energy ( $4.558$  eV) among the six structures.

Furthermore, the calculated total energy of the spin-polarized state is approximately  $132$  meV lower than that of the non-spin-polarized state for  $C_i-V_{Al}$ , indicating that  $C_i-V_{Al}$  prefers the spin-polarized state. The spin-polarized density of states (DOS) and partial DOS for C  $2p$  and N  $2p$  of  $C_i-V_{Al}$  are shown in Fig. 6. The total DOS indicates spin-polarized states around the Fermi level and an intermediate band (IB) in the bandgap. The spin-polarized states are mainly attributed to the  $2p$  electrons of N atoms, while the IB is attributed to the hybridization of C  $2p$  and N  $2p$  electrons. The IB is also spin polarized. The magnetic moment of  $C_i-V_{Al}$  mainly originates from the unpaired N  $2p$  electrons around the Al vacancy, and each N atom carries a magnetic moment of  $0.26 \mu_B$ . Compared to other AlN:C defects containing C atoms and Al vacancies, the  $C_i-V_{Al}$  defect complexes are more likely to form in the C<sup>+</sup>-implanted AlN films, contributing to the ferromagnetism. The results of the first-principles calculations suggest that the ferromagnetism in the C<sup>+</sup>-implanted AlN films originates from the  $C_i-V_{Al}$  defect complexes.

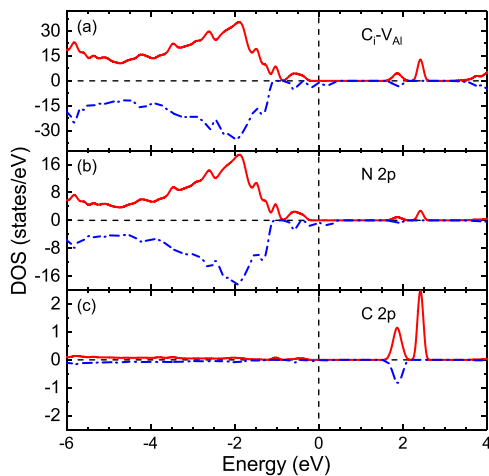
In summary, room-temperature ferromagnetism was observed in the C<sup>+</sup>-implanted AlN films. Magnetic measurements revealed that the  $M_S$  value of the C<sup>+</sup>-implanted AlN films depends on the dose of C<sup>+</sup> ions. XRD measurements demonstrated that the C atoms substitute at the sites of the Al atoms and occupy the interstitial sites after



**FIG. 5.** Top views of the  $3 \times 3 \times 2$  AlN supercells containing (a) an Al vacancy ( $V_{Al}$ ), (b) an interstitial C atom ( $C_i$ ), (c) a substitutional C atom at an Al site ( $C_{Al}$ ), (d) an interstitial-vacancy complex ( $C_i-V_{Al}$ ), (e) a substitutional-vacancy complex ( $C_{Al}-V_{Al}$ ), and (f) an interstitial-vacancy/substitutional complex ( $C_i-V_{Al}-C_{Al}$ ). The red dashed circles represent the sites of Al vacancies.

**TABLE II.** Total magnetic moments and the formation energies of the AlN structures with different defects.

System	$V_{Al}$	$C_i$	$C_{Al}$	$C_i-V_{Al}$	$C_{Al}-V_{Al}$	$C_i-V_{Al}-C_{Al}$
$m$ ( $\mu_B$ )	3.00	2.00	0.00	1.00	2.00	0.00
$E_f$ (eV)	6.902	7.043	5.432	4.558	8.371	12.357



**FIG. 6.** (a) Total DOS of the AlN supercell with the  $V_{Al}-C_i$  structure. Partial DOS of (b) N 2p electrons and (c) C 2p electrons. The vertical dashed line represents the Fermi level. The red solid (blue dash-dotted) lines refer to the spin-up (spin-down) components.

implantation. Moreover, XPS and DBAR measurements suggested that the Al-related vacancies were introduced in the  $C^+$ -implanted AlN films through ion implantation. The first-principles calculations revealed that the ferromagnetism originates mainly from the defect complexes involving the interstitial C atoms and the Al vacancies. The interstitial C atoms cause the formation energy of the Al vacancies to decrease, leading to high concentrations of the  $C_i - V_{Al}$  defect complexes. This work provides further insight into the roles of cation vacancies and interstitial atoms in ferromagnetism within the nonmagnetic element-implanted DMSs.

See the [supplementary material](#) for details regarding the SRIM simulations and the first-principles calculations.

We are grateful for helpful discussions with Dr. J. Zeng about the first-principles calculations. This work was supported by the National R&D Program of China (Grant No. 2019YFA0210000) and the National Natural Science Foundation of China (Grant Nos. 11775215, 11875248, and 11975225).

## REFERENCES

- 1S. Wolf, D. Awschalom, R. Buhrman, J. Daughton, S. Von Molnar, M. Roukes, A. Y. Chtchelkanova, and D. Treger, *Science* **294**, 1488 (2001).
- 2K. Ueda, H. Tabata, and T. Kawai, *Appl. Phys. Lett.* **79**, 988 (2001).
- 3Y. Matsumoto, M. Murakami, T. Shono, T. Hasegawa, T. Fukumura, M. Kawasaki, P. Ahmet, T. Chikyow, S.-Y. Koshihara, and H. Koinuma, *Science* **291**, 854 (2001).
- 4S. Ogale, R. Choudhary, J. Buban, S. Lofland, S. Shinde, S. Kale, V. Kulkarni, J. Higgins, C. Lanci, J. Simpson *et al.*, *Phys. Rev. Lett.* **91**, 077205 (2003).
- 5M. Reed, N. El-Masry, H. Stadelmaier, M. Ritums, M. Reed, C. Parker, J. Roberts, and S. Bedair, *Appl. Phys. Lett.* **79**, 3473 (2001).
- 6J. Xu, Q. Li, W. Zhang, J. Liu, H. Du, and B. Ye, *Chem. Phys. Lett.* **616-617**, 161 (2014).
- 7R. Frazier, G. Thaler, J. Leifer, J. Hite, B. Gila, C. Abernathy, and S. Pearton, *Appl. Phys. Lett.* **86**, 052101 (2005).
- 8R. Frazier, G. Thaler, M. Overberg, B. Gila, C. Abernathy, and S. Pearton, *Appl. Phys. Lett.* **83**, 1758 (2003).
- 9X. Gao, E. Jiang, H. Liu, W. Mi, Z. Li, P. Wu, and H. Bai, *Appl. Surf. Sci.* **253**, 5431 (2007).
- 10H. Liu, S. Y. Wu, R. Singh, L. Gu, D. J. Smith, N. Newman, N. Dilley, L. Montes, and M. Simmonds, *Appl. Phys. Lett.* **85**, 4076 (2004).
- 11J. Xiong, P. Guo, Y. Cai, B. Stradel, J. Brumek, Y. He, and H. Gu, *J. Alloys Compd.* **606**, 55 (2014).
- 12M. van Schilfgaarde and O. Mryasov, *Phys. Rev. B* **63**, 233205 (2001).
- 13J. Zhang, X. Li, B. Xu, and D. J. Sellmyer, *Appl. Phys. Lett.* **86**, 212504 (2005).
- 14K. Li, X. Du, Y. Yan, H. Wang, Q. Zhan, and H. Jin, *Phys. Lett. A* **374**, 3671 (2010).
- 15C. Liu, B. Mensching, K. Volz, and B. Rauschenbach, *Appl. Phys. Lett.* **71**, 2313 (1997).
- 16See <https://xpspeak.software.informer.com/> for the detail about XPSPEAK 4.1 software.
- 17T. Lay, W. Kuo, L. Chen, Y. Lai, W.-H. Hung, J. Wang, J. Chi, D. Shih, and H. Lin, *J. Vac. Sci. Technol., B* **22**, 1491 (2004).
- 18M. Petracic, P. N. Deenanaray, V. A. Coleman, K.-J. Kim, B. Kim, and G. Li, *J. Appl. Phys.* **95**, 5487 (2004).
- 19L. Zhang, C. Zhang, C. Li, Y. Song, Y. Jin, and T. Wang, *Eur. Phys. J.* **59**, 30101 (2012).
- 20J.-D. Hecht, F. Frost, D. Hirsch, H. Neumann, A. Schindler, A. Preobrajenski, and T. Chassé, *J. Appl. Phys.* **90**, 6066 (2001).
- 21Y. Wang, Y. Shao, S. Hsieh, Y. Chang, P. Yeh, H. Hsueh, J. Chiou, H. Wang, S. Ray, H. Tsai *et al.*, *Sci. Rep.* **8**, 7758 (2018).
- 22B. Zhang, B. Yao, Y. Li, A. Liu, Z. Zhang, B. Li, G. Xing, T. Wu, X. Qin, D. Zhao *et al.*, *Appl. Phys. Lett.* **99**, 182503 (2011).
- 23F. Tuomisto, *J. Phys. Conf. Ser.* **265**, 012003 (2011).
- 24O. Yildirim, S. Cornelius, M. Butterling, W. Anwand, A. Wagner, A. Smekhova, J. Fiedler, R. Böttger, C. Bähz, and K. Potzger, *Appl. Phys. Lett.* **107**, 242405 (2015).
- 25A. Uedono, K. Ito, H. Nakamori, K. Mori, Y. Nakano, T. Kachi, S. Ishibashi, T. Ohdaira, and R. Suzuki, *J. Appl. Phys.* **102**, 084505 (2007).
- 26X. Li, Z. Chen, C. Liu, H. Zhang, and A. Kawasuso, *J. Appl. Phys.* **117**, 085706 (2015).
- 27J. Gebauer, F. Börner, R. Krause-Rehberg, T. Staab, W. Bauer-Kugelmann, G. Kögel, W. Triftshäuser, P. Specht, R. Lutz, E. Weber *et al.*, *J. Appl. Phys.* **87**, 8368 (2000).
- 28J. Chen, Z. Wan, J. Liu, S.-Q. Fu, F. Zhang, S. Yang, S. Tao, M. Wang, and C. Chen, *ACS Appl. Mater. Interfaces* **10**, 8649 (2018).
- 29H. Li, W. Wang, and G. Cai, *J. Magn. Magn. Mater.* **460**, 391 (2018).
- 30H. Schulz and K. Thiemann, *Solid State Commun.* **23**, 815 (1977).
- 31R. Wu, G. Peng, L. Liu, Y. Feng, Z. Huang, and Q. Wu, *Appl. Phys. Lett.* **89**, 142501 (2006).